Short Article

Cell Metabolism

Long-Term Cold Adaptation Does Not Require FGF21 or UCP1

Graphical Abstract

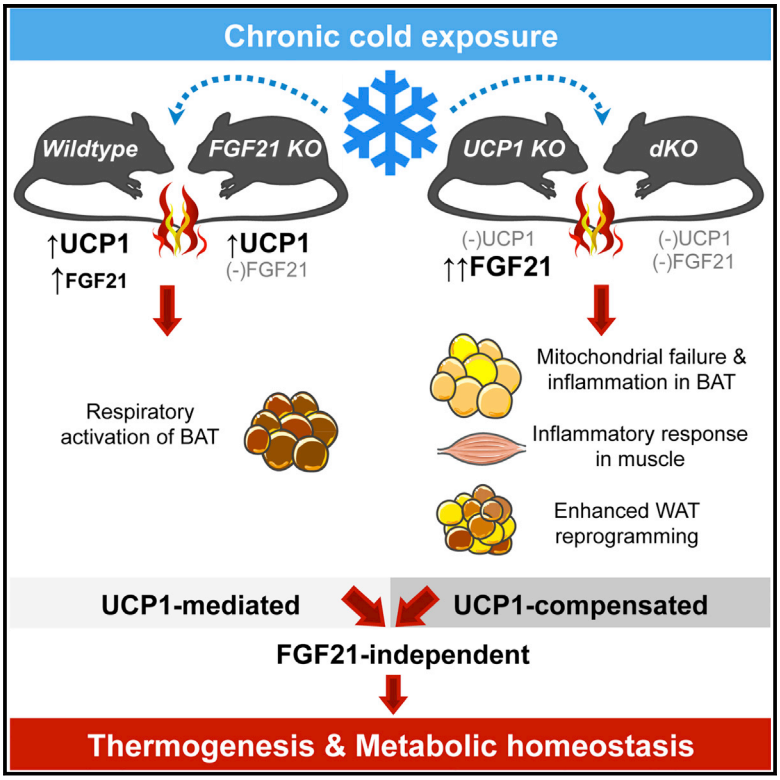

Highlights

- UCP1 and/or FGF21 are not required for metabolic homeostasis in chronic cold
- Mitochondrial failure and inflammatory signals in UCP1-ablated BAT
- FGF21-independent "browning" of white adipose tissue in the cold
- Bioenergetic evaluation of "putative alternative heating pathways" in beige adipocytes

Authors

Susanne Keipert, Maria Kutschke, Mario Ost, ..., Frauke Neff, Matthias H. Tschöp, Martin Jastroch

Correspondence

martin.jastroch@helmholtz-muenchen.de

In Brief

Using UCP1-FGF21 double-knockout mice, Keipert et al. report that neither UCP1 nor FGF21, nor even compensatory increases of FGF21 serum levels in UCP1 knockout mice, are required for defense of body temperature or for maintenance of energy metabolism and body weight.

Keipert et al., 2017, Cell Metabolism *26*, 437–446
August 1, 2017
http://dx.doi.org/10.1016/j.cmet.2017.07.016

Cell Metabolism
Short Article

Long-Term Cold Adaptation Does Not Require FGF21 or UCP1

Susanne Keipert,[1,2] Maria Kutschke,[1] Mario Ost,[3] Thomas Schwarzmayr,[4] Evert M. van Schothorst,[5] Daniel Lamp,[1] Laura Brachthäuser,[6] Isabel Hamp,[7,8] Sithandiwe E. Mazibuko,[1] Sonja Hartwig,[2,9] Stefan Lehr,[2,9] Elisabeth Graf,[4] Oliver Plettenburg,[7,8] Frauke Neff,[6] Matthias H. Tschöp,[1,2,11] and Martin Jastroch[1,2,10,12,*]

[1]Institute for Diabetes and Obesity, Helmholtz Diabetes Center, German Research Center for Environmental Health (GmbH), Neuherberg, Germany
[2]German Center for Diabetes Research (DZD), Neuherberg, Germany
[3]German Institute of Human Nutrition, Nuthetal, Germany
[4]Institute of Human Genetics, Helmholtz Zentrum München, German Research Center for Environmental Health (GmbH), Neuherberg, Germany
[5]Human and Animal Physiology, Wageningen University, Wageningen, the Netherlands
[6]Institute of Pathology, Helmholtz-Zentrum München, German Research Center for Environmental Health (GmbH), Neuherberg, Germany
[7]Institute of Medicinal Chemistry, Helmholtz Zentrum München, German Research Center for Environmental Health (GmbH), Neuherberg, Germany
[8]Institute of Organic Chemistry, Leibniz Universität Hannover, Hannover, Germany
[9]Institute for Clinical Biochemistry and Pathobiochemistry, German Diabetes Center (DDZ), Düsseldorf, Germany
[10]Department of Animal Physiology, Faculty of Biology, Philipps University of Marburg, Marburg, Germany
[11]Division of Metabolic Diseases, Department of Medicine, Technische Universität München, München, Germany
[12]Lead Contact
*Correspondence: martin.jastroch@helmholtz-muenchen.de
http://dx.doi.org/10.1016/j.cmet.2017.07.016

SUMMARY

Brown adipose tissue (BAT)-dependent thermogenesis and its suggested augmenting hormone, FGF21, are potential therapeutic targets in current obesity and diabetes research. Here, we studied the role of UCP1 and FGF21 for metabolic homeostasis in the cold and dissected underlying molecular mechanisms using UCP1-FGF21 double-knockout mice. We report that neither UCP1 nor FGF21, nor even compensatory increases of FGF21 serum levels in UCP1 knockout mice, are required for defense of body temperature or for maintenance of energy metabolism and body weight. Remarkably, cold-induced browning of inguinal white adipose tissue (iWAT) is FGF21 independent. Global RNA sequencing reveals major changes in response to UCP1- but not FGF21-ablation in BAT, iWAT, and muscle. Markers of mitochondrial failure and inflammation are observed in BAT, but in particular the enhanced metabolic reprogramming in iWAT supports the thermogenic role of UCP1 and excludes an important thermogenic role of endogenous FGF21 in normal cold acclimation.

INTRODUCTION

In small mammals, including human infants, mitochondrial uncoupling protein 1 (UCP1) of brown adipose tissue (BAT) provides the primary mechanism for adaptive non-shivering thermogenesis (NST) to defend body temperature at cold ambient temperatures (Cannon and Nedergaard, 2004). Given its presence in adult humans (Nedergaard et al., 2007), active BAT could impact body weight (Matsushita et al., 2014).

The classical mechanism of NST through UCP1 occurs not only in brown but also in so-called "beige" (or "brite") adipose tissue (Shabalina et al., 2013). Beige adipocytes are characterized by multilocular lipid droplet morphology, thermogenic capacity, and compared to white adipocytes, higher mitochondrial content (Keipert and Jastroch, 2014). Beige cells develop within white adipose tissue (WAT), a process termed "browning," in response to various stimuli, i.e., cold, dietary interventions, or pharmacological treatments (Fabbiano et al., 2016; Fisher et al., 2012; Vitali et al., 2012). Impressively, severe paucity of BAT in Myf5-BMPR1A knockout mice is compensated by browning of WAT, which was interpreted as sufficient for restoration of total BAT-mediated thermogenic capacity (Schulz et al., 2013). Recent work from Spiegelman and colleagues suggested two UCP1-independent thermogenic pathways in beige cells (Kazak et al., 2015; Long et al., 2016), highlighting alternative mechanisms of thermogenesis. However, as shivering is still induced in UCP1 knockout (UCP1 KO) mice in the cold, alternative pathways cannot fully replace UCP1. A potent enhancer of WAT browning is circulating fibroblast growth factor 21 (FGF21), an important metabolic regulator and a potential therapeutic target for the treatment of obesity and diabetes (Coskun et al., 2008; Fisher et al., 2012; Kharitonenkov et al., 2007). Some analyses of metabolic rate suggest increases in energy expenditure in response to FGF21 administration (e.g., Samms et al., 2015), although there could be confounding effects of body weight reduction. However, FGF21's role in thermogenesis is not completely understood, as increased energy expenditure appears to be independent of UCP1 to a large extent (Samms et al., 2015). Given that cold exposure increases FGF21

expression in WAT and BAT, there are several claims that FGF21 improves BAT function, in addition to mediating other metabolic effects. In rodents, FGF21 is induced in and released from BAT in response to cold exposure, thus strongly suggesting a regulatory role of FGF21 in adaptive thermogenesis (Chartoumpekis et al., 2011; Fisher et al., 2012; Hondares et al., 2011; Keipert et al., 2015). Furthermore, FGF21 KO mice show larger lipid droplets in BAT, possibly due to less active energy turnover (Badman et al., 2009). These mice appeared to be cold intolerant, suggesting a profound requirement for FGF21 during BAT thermogenesis (Fisher et al., 2012). In humans, mild cold exposure increases circulating FGF21 levels (Lee et al., 2013) and cold-induced circulating FGF21 levels are associated with BAT activity (Hanssen et al., 2015; Lee et al., 2014). The importance of FGF21 for BAT thermogenesis is further fostered by dramatically potentiated FGF21 release in BAT of UCP1 KO mice below thermoneutrality (Keipert et al., 2015). Although UCP1 KO mice are sensitive to acute cold exposure, they are able to survive stepwise cold acclimation with no obvious metabolic disadvantages (Golozoubova et al., 2001; Meyer et al., 2010; Ukropec et al., 2006). Intriguingly, cold-adapted UCP1 KO mice display morphological and molecular changes in WAT that resemble typical FGF21 browning effects (Granneman et al., 2003; Keipert et al., 2015; Ukropec et al., 2006). Thus, the cumulative evidence from rodent and human studies suggests a key role for FGF21 in UCP1-mediated as well as UCP1-independent regulation of adaptive thermoregulation, possibly by mediating endocrine cross-talk between (inactive) BAT and other potentially thermogenic tissues (e.g., WAT).

In this study, we directly tested for the relevance of FGF21 in combination with UCP1 in the cold by comprehensive metabolic phenotyping using wild-type (WT), FGF21 KO, UCP1 KO, and UCP1-FGF21 double-knockout mice (dKO) mice. First, we confirmed that UCP1 KO mice display elevated serum FGF21, released from BAT during cold exposure (Keipert et al., 2015). Using established protocols for cold acclimation, a 2-week period of mild cold preconditioning at 18°C was followed by 5°C cold exposure for 3 weeks with continuous recordings of metabolic activity and body temperature. To elucidate the underlying molecular mechanisms, we performed global RNA sequencing of four major tissues. Our data highlight that cold exposure is a powerful environmental stimulus enhancing thermogenesis and energy expenditure to defend body temperature even in the absence of UCP1 and FGF21, potentially supported by molecular pathways in WAT.

RESULTS AND DISCUSSION

Adipose Tissue FGF21 Expression Is Augmented in UCP1 KO Mice during Cold

Consistent with previously published data (Fisher et al., 2012; Hondares et al., 2011) liver *Fgf21* gene expression is not induced by chronic cold stress, in contrast to strong upregulation in BAT (40-fold) and WAT (5-fold), reaching levels found in the liver of WT mice (Figure 1A). Importantly, UCP1 KO mice potently elevate *Fgf21* mRNA in BAT and inguinal WAT (iWAT), showing induction levels of more than 1,000-fold and 100-fold, respectively (Figure 1B).

To evaluate the role of FGF21 in UCP1 KO mice, we have generated UCP1-FGF21 dKO mice (and WT, FGF21 KO, and UCP1 KO) at thermoneutrality and challenged all four genotypes with prolonged cold exposure of 5°C for 3 weeks (Figure 1C). The simultaneous inactivation of *Ucp1* and *Fgf21* gene expression was consolidated with qPCR of BAT and iWAT samples (Figures 1D and 1E). Notably, *Ucp1* mRNA levels are not impacted by the absence of FGF21 (WT versus FGF21 KO, Figure 1D). In line with previous findings (Keipert et al., 2015), elevated *Fgf21* mRNA in BAT and iWAT is associated with elevated circulating FGF21 serum levels in UCP1 KO mice (Figure 1F), suggesting endocrine cross-talk of BAT with other tissues, putatively recruiting metabolic pathways that compensate the lack of classical UCP1-mediated NST. All cold-acclimated mice display no differences in blood glucose and lactate levels (Figure S1A). In the absence of UCP1, independent of FGF21 levels, serum lipids, are decreased, but not cholesterol and adiponectin (Figures S1B and S1C). There was no differential regulation of selected inflammatory cytokines (Figure S1D) and myo-/adipokines (Figure S1E) in blood serum.

FGF21 and/or UCP1 Do Not Impact Metabolic Phenotypes

We tracked body weight and simultaneously measured body temperature, energy expenditure, food intake, and activity to determine the role of the UCP1-FGF21 axis in energy balance and adaptive thermogenesis. Mice of all four genotypes were continuously recorded during the decrease of ambient temperature from 30°C (thermoneutrality) to 18°C for 12 days, followed by 3 weeks at 5°C. No difference in any of the measured metabolic parameters was observed between WT and FGF21 KO mice (Figures 2A, 2C, 2E, and 2G), which corroborates the negligible role of FGF21 in adaptive NST of mice. Body weight, possibly the most sensitive parameter reporting changes in energy balance, does not reveal any genotypic differences and remains fairly stable during cold acclimation (Figures 2A and 2B). Given the tripling of food intake from 30°C to 5°C to compensate for heat loss, the genetic ablation of UCP1 and/or FGF21 has minor impact on food intake (Figures 2A and 2B). All genotypes reduce activity in the scotophase in response to decreasing ambient temperature (Figures 2A and 2B), with enhanced depression of activity in the absence of UCP1 only during moderate cold exposure (18°C). Changing ambient temperature from 30°C to 18°C leads to an increased day/night amplitude in the 48-hr time course of the respiratory quotient (RQ; Figures 2C and 2D), demonstrating metabolic flexibility during cold of all genotypes (i.e., fast switch between carbohydrate and lipid oxidation). At 5°C, the mean value of the RQ is not different between the genotypes, while the lower amplitude seen in the 48-hr time course hints to less flexibility in fuel preference during daytime in UCP1 KO and dKO mice (Figures 2C and 2D).

Previously, Fisher et al. showed that the ablation of FGF21 leads to an impaired response to cold stress when placing mice from 27°C to 5°C for 3 days (Fisher et al., 2012). Our cold-acclimation protocol does not impair body temperature in FGF21 KO mice (Figure 2E) at any time during 36 days of measurement, suggesting that FGF21 plays no role during long-term adaptive thermoregulation. Core body temperature during daytime decreases in WT and FGF21 KO mice at 5°C (Figure 2E),

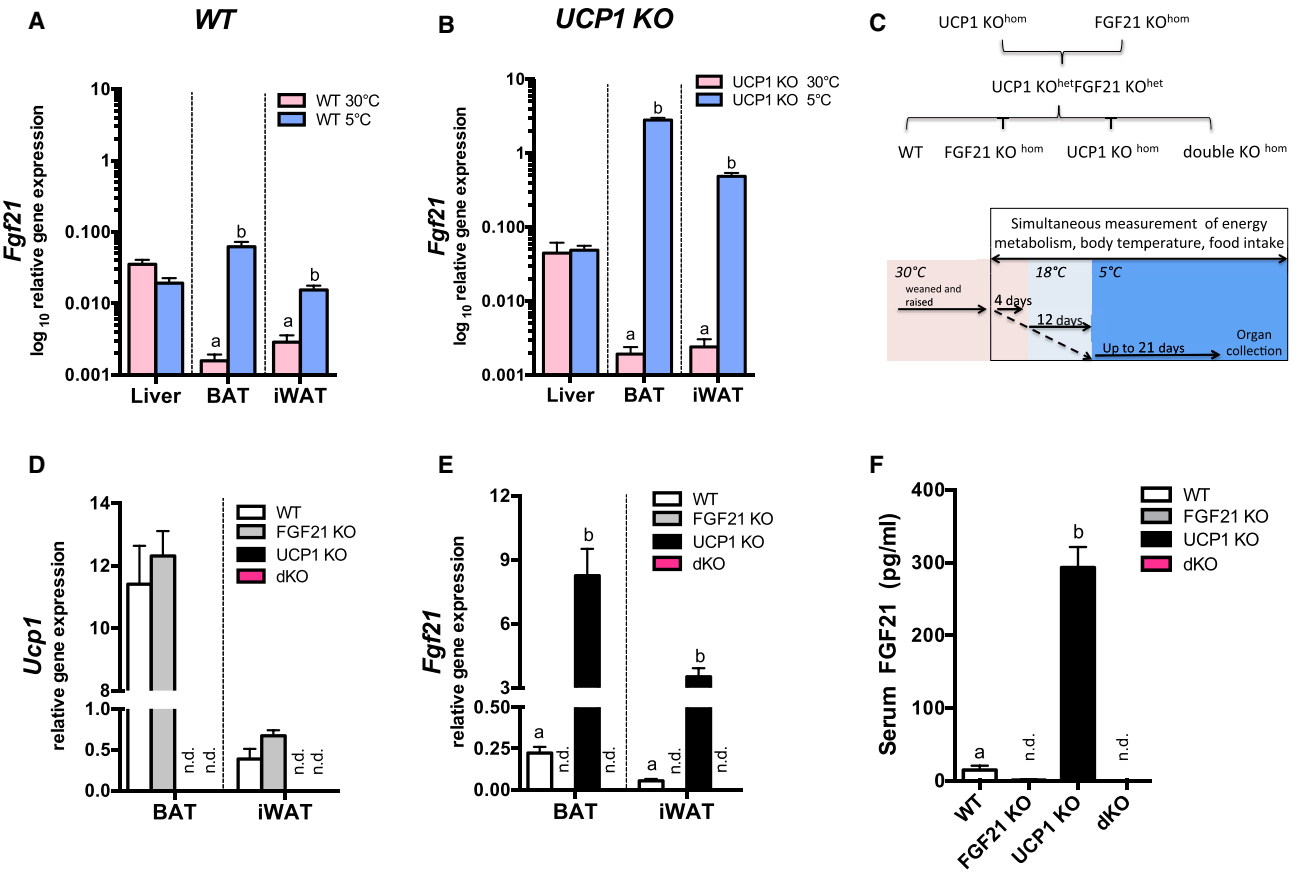

Figure 1. Augmented FGF21 Levels in Mice Lacking UCP1 and Generation of FGF21-UCP1 Double-Knockout Mice

(A and B) *Fgf21* mRNA in liver, BAT, and iWAT of WT mice (A) or UCP1 KO mice (B) kept at 30°C or at 5°C for 3 weeks (upon acclimation to 18°C for 12 days).

(C) Breeding scheme of the FGF21-UCP1 dKO cohort and schematic illustration of cold acclimation.

(D–F) *Fgf21* gene expression (D) and *Ucp1* gene expression (E) as well as FGF21 serum levels (F) in WT, FGF21 KO, UCP1 KO, and dKO mice upon cold exposure. n.d., not detectable; data represent means ± SEM (n = 6–8). Statistical differences ($p < 0.05$) are indicated by different letters. See also Figure S1.

but not in UCP1 KO and dKO mice (Figure 2F). The periodically increased body temperature in the absence of functional BAT may be explained by altered heat distribution.

Analysis of energy expenditure shows the expected increases in response to cold, but reveals no genotypic differences (Figures 2G and 2H), unequivocally demonstrating that global metabolic homeostasis during cold is maintained irrespective of UCP1 or/and FGF21. Plotting body weight versus energy expenditure reveals no genotypic difference in body-weight-dependent energy expenditure (Figure 2I), suggesting that alternative thermoregulatory pathways are not more costly for systemic thermoregulation than UCP1-mediated heat production. Taken together, the phenotypic data demonstrate that the role of FGF21 in maintaining body temperature after prolonged cold exposure is dispensable, even in the absence of UCP1.

Minor Impact of FGF21 in UCP1-Dependent and -Independent BAT Biology in the Cold

Given the predominant thermogenic role of UCP1, as well as the suggested impact of FGF21 in BAT and beige adipose tissue, we focus here on the genotypic effects on adipose tissue morphology and gene regulation. While the morphology of BAT differs dramatically between the genotypes (Figures 3A and 3B), there were no differences in total BAT weight (Figures 3C and 3D; dashed line indicates WT mean value). No changes in morphology between WT and FGF21 KO mice (left panels) are observed in this study, consistent with unchanged UCP1 protein levels and *Ppargc1A*, *Dio2*, and *Cidea* gene expression (Figure 3C), as well as unchanged protein levels of representative respiratory chain subunits (Figure 3E). Together, these data point to a minor role of FGF21 in cold-induced BAT thermogenesis, at least during long-term exposure. In contrast to WT and FGF21 mice, BAT of UCP1 KO mice displays a higher density of unilocular fat cells, a typical WAT feature (Figure 3B). Notably, the additional inactivation of FGF21 (in dKO mice) results in a drastically reduced number of lipid droplets. Interestingly, only the lack of both UCP1 and FGF21 is responsible for a mildly increased expression of *Dio2* (Figure 3D). Remarkably, the lack of UCP1 in BAT per se promotes a strong reduction of respiratory chain complexes (Figure 3F; dashed line: WT mean), supporting the conclusion that oxidative BAT thermogenesis has limited significance. A very recent study shows similar reductions of respiratory chain complexes (Kazak et al., 2017). These findings of both independent studies provide the molecular rationale for reduced

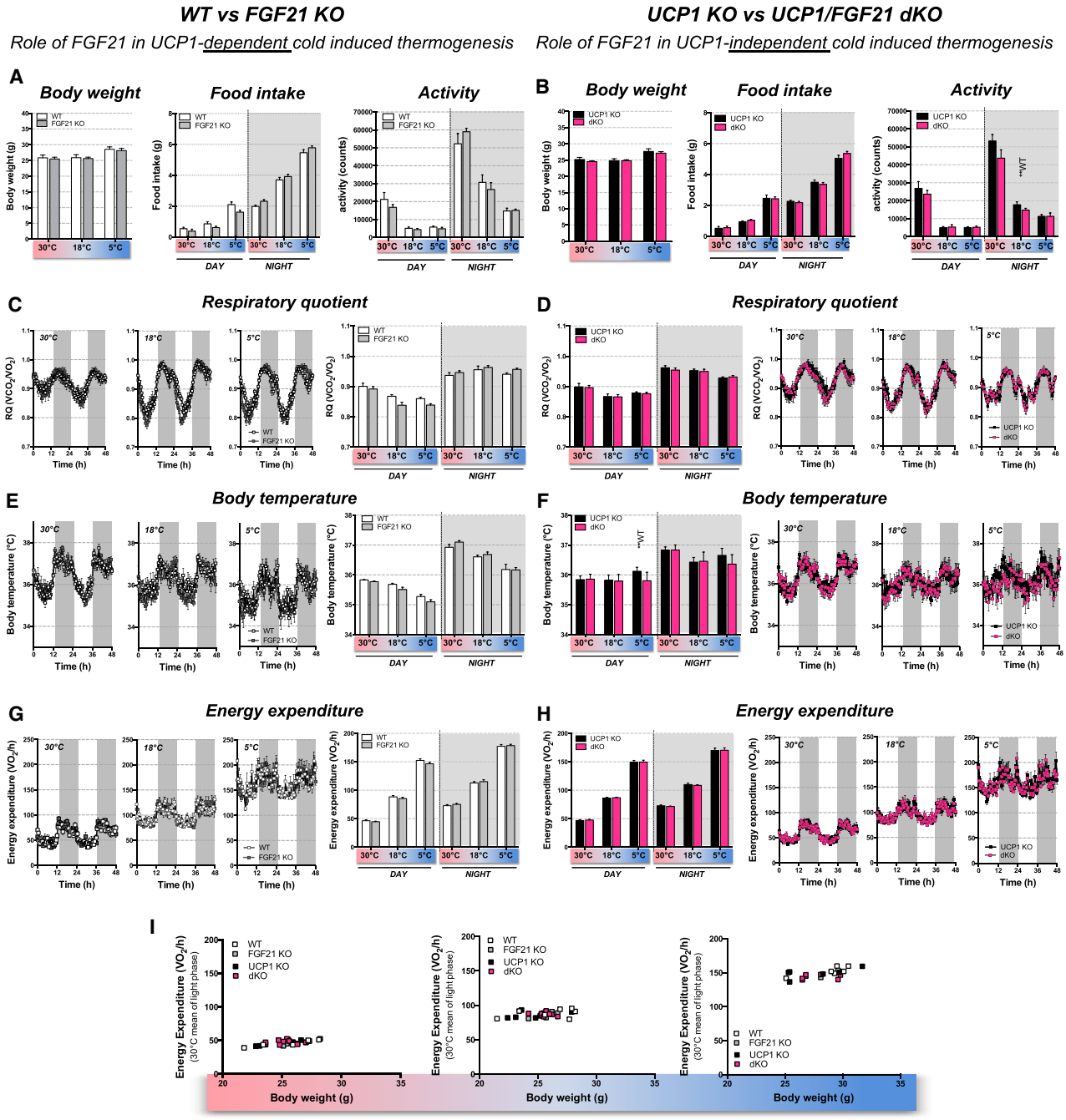

Figure 2. The Lack of FGF21 and/or UCP1 Does Not Impact Metabolic Mouse Phenotypes upon Cold Acclimation

(A and B) Body weight, food intake, and activity of warm (30°C), moderate cold (18°C), and cold (5°C) acclimated WT, FGF21 KO, UCP1 KO, and dKO mice. (C–H) Respiratory quotient (C and D), body temperature (E and F), and energy expenditure (G and H) are shown as longitudinal (last 2 days of each temperature step) and means (±SEM).

(I) Mean energy expenditure data are plotted against body weight. Statistically significant differences between WT and UCP1 KO or dKO are denoted by WT $^{**}p < 0.01$ ($n = 6–8$).

respiration in UCP1-ablated BAT mitochondria (Oelkrug et al., 2010). To fully understand the molecular impact of FGF21 and UCP1, whole-transcriptome analysis was performed for cold-acclimated mice. The top 30 significantly up- and downregulated (FDR-adjusted $p < 0.05$) genes are visualized as heatmap on the basis of hierarchical clustering (Figure 3G). Principal component analysis (PCA) and Venn diagrams of significant regulated genes (FC ≥ 1.2; FDR-adjusted $p < 0.05$) illustrate the separation of the four genotypes into two major groups (WT/FGF21 KO and UCP1 KO/dKO), thus elucidating major transcriptomic changes

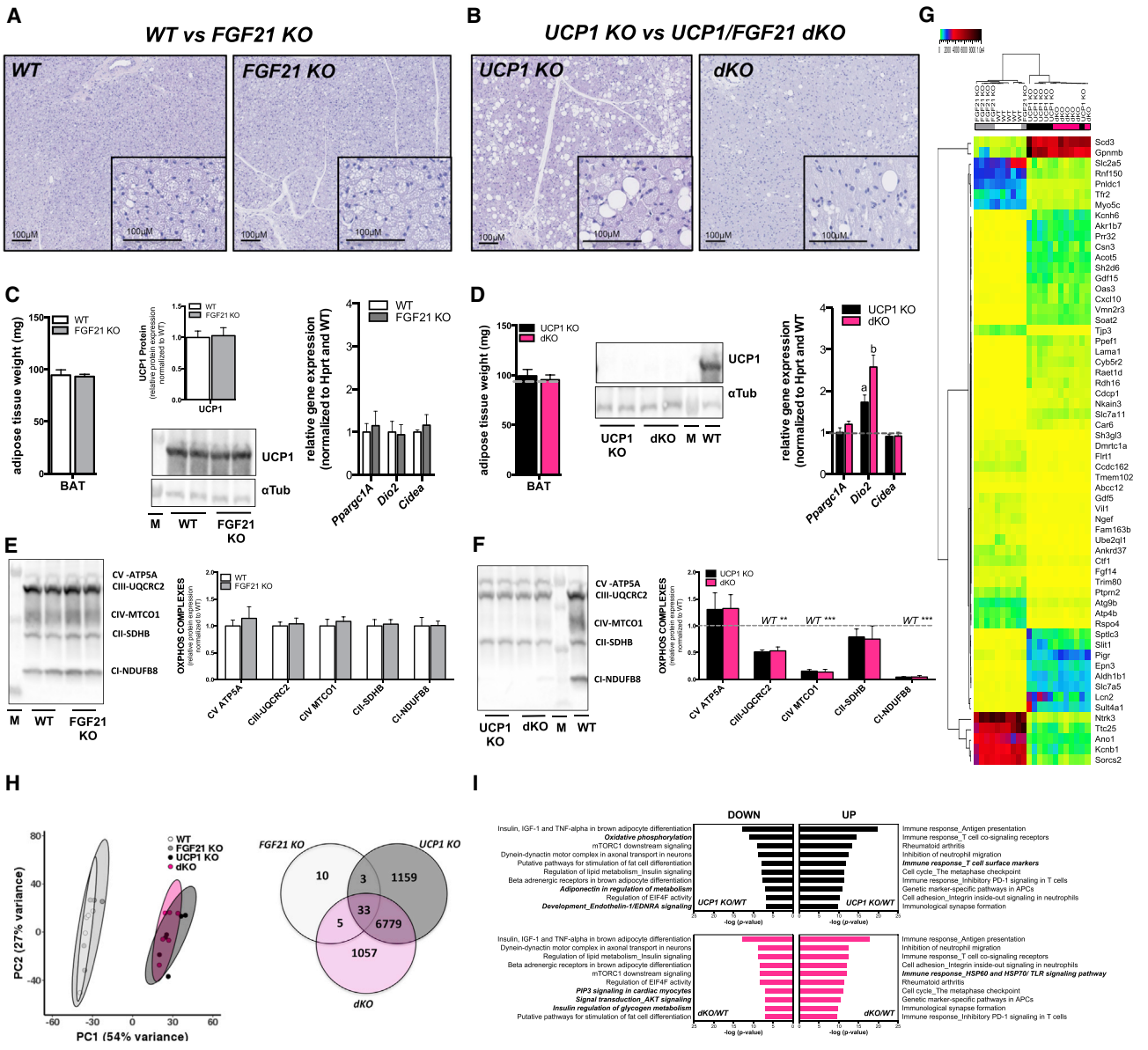

Figure 3. Minor Impact of FGF21 in UCP1-Dependent and -Independent BAT Biology in the Cold

(A–F) Morphology (A and B); tissue weight, UCP1 protein levels, and gene expression of *Dio2*, *Cidea*, and *Ppargc1a* (C and D); and protein levels of respiratory chain complexes in BAT of long-term cold-exposed WT, FGF21 KO, UCP1 KO, and dKO mice (E and F). M, molecular weight marker; data represent means ± SEM (n = 6–8). Statistically significant differences between WT and UCP1 KO or dKO are denoted by WT $^{**}p < 0.01$, WT $^{***}p < 0.001$ (gray dashed line indicates WT value), and statistically significant differences ($p < 0.05$) between UCP1 KO and dKO are denoted by different letters.

(G–I) Transcriptomic analysis for FGF21- and/or UCP1-dependent remodeling of BAT from long-term cold-exposed animals (n = 5–6). (G) The top30 up- and downregulated unique transcripts between WT and UCP1 KO were determined. The heatmap illustrates relative expression of all genotypes. (H) PCA of all genes demonstrating the distinct profile of WT/FGF21 KO versus UCP1 KO/dKO mice. The Venn diagram depicts overlaps of significantly altered gene expression between genotypes (FC ≥ 1.2; $p < 0.05$ FDR-adjusted).

(I) Pathway enrichment analysis (using MetaCore) depicts the top 10 upregulated (right) or downregulated (left) pathways (UCP1 KO/WT; dKO/WT; exclusive pathways highlighted in bold). See also Figure S2.

through the lack of UCP1 and the negligible impact of FGF21 in BAT during chronic cold (Figure 3H). Notably, the top enriched pathways uncover pronounced immune responses and the reduction of oxidative metabolism in the absence of UCP1 (Figure 3I). The transcriptomes of hypothalamus and skeletal muscle, two other important tissues for thermoregulation, reveal no major FGF21-dependent changes (Figures S2A and S2B). While PCA of hypothalamic gene expression shows no genotypic clustering, the lack of UCP1 affects the muscle transcriptome (Figures S2B and S2C), possibly through adaptation to enhanced shivering, as suggested by others (Golozoubova et al., 2001). Similar to BAT, FGF21-independent immune responses in

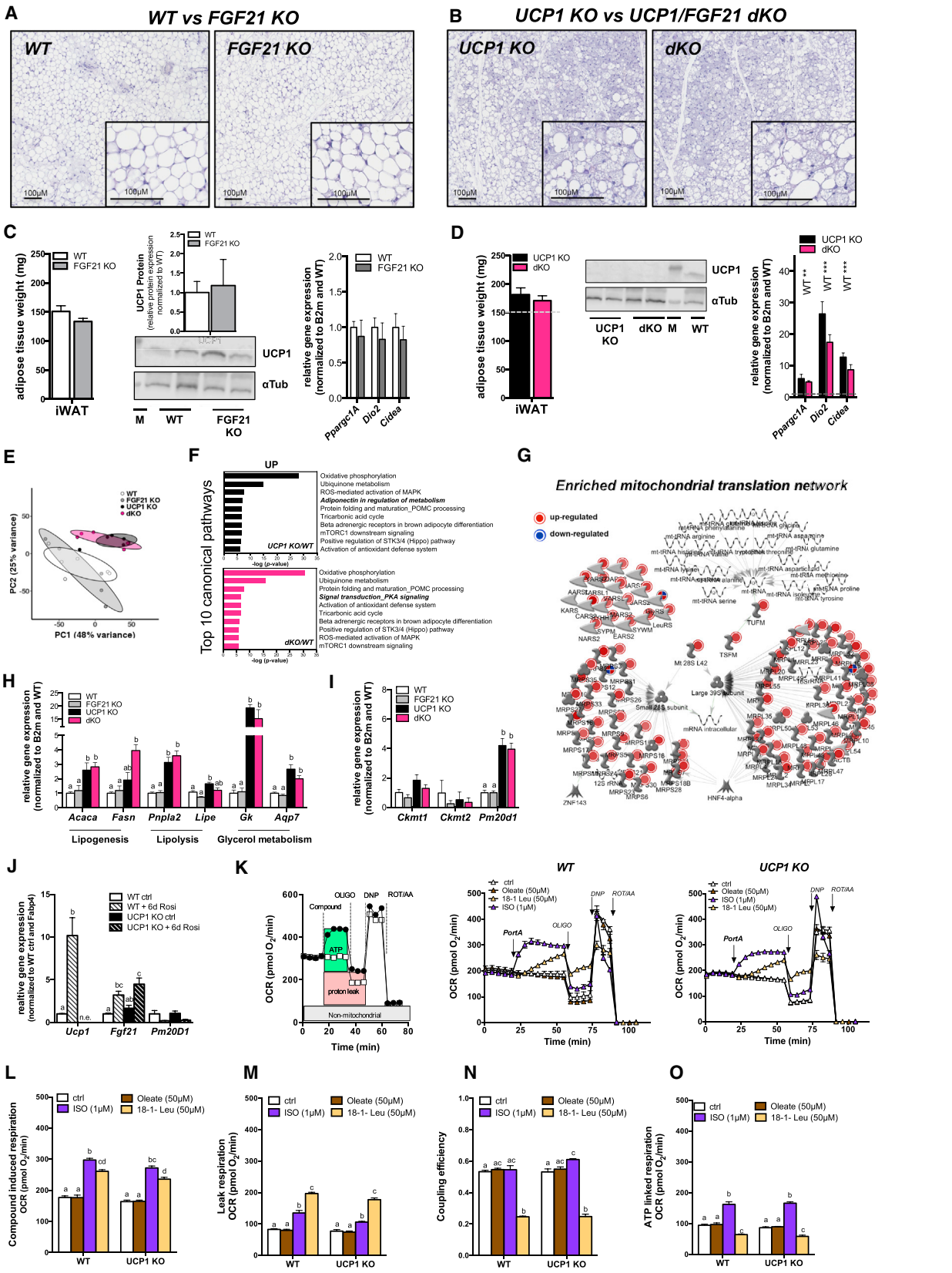

(legend on next page)

skeletal muscle of UCP1 KO versus WT mice are observed in the top enriched pathways (Figure S2D), possibly reporting dysfunctional cellular properties in muscle, such as oxidative stress (Stier et al., 2014) or defective calcium handling (Aydin et al., 2008). Furthermore, the gene expression profile of UCP1 KO and dKO muscles suggests increased lipid metabolism and slightly shifted muscle fiber type, typical adjustments of muscle training and shivering (Shabalina et al., 2010) (Figures S2E and S2F). However, muscle mass was unchanged (Figure S2G).

WAT Remodeling and Potential Sources of Heat

Besides BAT and muscle, iWAT has been suggested as a potential site of thermogenesis during cold acclimation. WT and FGF21 KO mice display no differences in iWAT morphology and weight, UCP1 protein, and mRNA levels of *Dio2*, *Cidea*, and *Ppargc1A* (Figures 4A and 4C), demonstrating that cold-induced browning of iWAT is not regulated via FGF21. Enhanced multilocularity and mildly increased iWAT weight in UCP1 KO mice (Figures 4B and 4D) are expected considering previous studies (Granneman et al., 2003; Keipert et al., 2015; Ukropec et al., 2006). WAT is a primary target of FGF21 action, inducing browning, glucose uptake (Kharitonenkov et al., 2005; Ost et al., 2015), and lipolysis (Inagaki et al., 2007). Given highly elevated circulating FGF21 levels in UCP1 KO mice (Figure 1), it is surprising that the additional deletion of FGF21 does not alter fat cell multilocularity of UCP1 KO mice (Figure 4B), suggesting that cold overrides FGF21 action to control metabolic homeostasis. Cold acclimation induces a morphological browning phenotype in iWAT of UCP1 KO and dKO mice. This browning is supported by significantly increased gene expression of the key thermogenic genes *Dio2*, *Ppargc1A*, and *Cidea* (Figure 4D; dashed line: WT mean). The additional deletion of FGF21 has no quantitative impact on thermogenic gene expression. The results of RNA sequencing are summarized as heatmap of the top 30 significantly up- and downregulated (FDR-adjusted $p < 0.05$) genes (Figure S3A). The PCA suggests only clear separation of UCP1-positive versus -negative samples (Figure 4E), supporting the minor role of FGF21 in the cold (Figure S3B). Pathway enrichment confirmed browning of iWAT in UCP1-ablated mice, suggesting increased metabolism by enrichment of oxidative phosphorylation and lipid metabolism (Figures 4F and S3C), as well as networks controlling mitochondrial translation (Figure 4G, S3D, and S3E). Additional qPCR analyses confirmed simultaneous upregulation of lipogenic and lipolytic as well as glycerol metabolism genes in UCP1-deficient mice (Figure 4H), suggesting increased lipid turnover (Haemmerle et al., 2011; Mottillo et al., 2014) or possibly futile lipid cycling as proposed by others (Guan et al., 2002; Rohm et al., 2016). Genes of creatine futile cycling, a recently proposed mechanism (Kazak et al., 2015), are not affected after prolonged cold (Figure 4I). However, *Pm20d1* gene expression, which results in an enzyme that has been suggested to generate n-acyl amino acids as endogenous uncouplers (Long et al., 2016), was selectively increased in iWAT of all UCP1-deficient mice (Figure 4I). Whether these molecular adaptations contribute to thermogenesis in the cold in the absence of UCP1 remains to be clarified. To at least estimate the functional relevance of endogenous uncouplers for adipocyte oxidative metabolism, we performed plate-based respirometry of immortalized browned adipocytes from WT and UCP1 KO mice (Figures 4J–4L and S4A–S4G). Mimicking the *in vivo* situation, *Fgf21* and *Ucp1* mRNA (Figures 4J and S4A) and detectable UCP1 protein (Figure S4B) were robustly induced by rosiglitazone treatment. *Pm20d1* mRNA was barely detectable in murine adipocytes in vitro (Figure 4J; C_T values 31–33). However, when testing exogenously n-acyl amino acids, the lack of gene expression formally excludes any experimental interference with endogenous Pm20d1. First, we synthetized n-acyl amino acids and confirmed that oleoyl-L-leucine uncouples mitochondria of intact WT and UCP1 KO adipocytes in state 4 (blocked ATP synthase), exceeding the effects of equimolar additions of oleate (Long et al., 2016) (Figures S4C and S4D). Interestingly, 50 μM and higher concentrations of various n-acyl amino acids decrease the thermogenic capacity in adipocytes, as judged by maximal respiration values induced with 2,4-Dinitrophenol (DNP) (Figures S4E–S4G). To assess the bioenergetic impact of the cold-mimetic isoproterenol and oleoyl-L-leucine at physiologically relevant conditions, compounds were injected without inhibition of ATP synthase (Figure 4K). While both compounds increase basal respiration to a similar extent (Figure 4L), oleoyl-L-leucine increases the mitochondrial proton leak more potently than isoproterenol

Figure 4. Minor Impact of FGF21 in UCP1-Dependent and -Independent Remodeling of iWAT and Bioenergetic Assessment of Potential Alternative Heat Sources in Browned Adipocytes In Vitro

(A–D) Morphology (A and B) and tissue weight, UCP1 protein levels, and gene expression (C and D) of *Dio2*, *Cidea*, and *Ppargc1a* in iWAT of long-term cold-exposed WT, FGF21 KO, UCP1 KO, and dKO mice. M, molecular weight marker; data represent means ± SEM (n = 6–8). Statistical significance between WT and UCP1 KO or dKO is denoted by WT $^{**}p < 0.01$, WT $^{***}p < 0.001$. The dashed line indicates WT mean value.

(E–G) Transcriptomic analysis for FGF21- and/or UCP1-dependent remodeling of iWAT from long-term cold-exposed animals (n = 5–6). (E) PCA of all genes demonstrating the distinct profile of WT/FGF21 KO versus UCP1 KO/dKO mice. (F) Pathway analysis (using MetaCore) depicts the top ten upregulated pathways of UCP1 KO/WT and dKO/WT (exclusive pathways highlighted in bold). (G) Process metabolic network analysis (using MetaCore) of genes encoding proteins involved in mitochondrial translation (red: upregulated in UCP1 KO mice compared to WT). Differently shaped nodes represent enzymes (arrows), ligands, and metabolites (hexagons) and other proteins (mirrored S-shapes).

(H) Expression of genes involved in lipid metabolism.

(I) *Ckmt1/2* and *Pm20d1* gene expression in iWAT (n = 6–8).

(J) *Ucp1*, *Fgf21*, and *Pm20d1* gene expression of immortalized inguinal white adipocytes (taken from WT and UCP1 KO mice), treated for 6 days with or without 1 μM rosiglitazone (n = 3).

(K) Respiration measurements to address "uncoupling" effects of N-acyl amino acids in vitro. Left panel: Scheme of oxygen consumption rate (OCR) time course illustrating mitochondrial and non-mitochondrial OCR and ATP synthesis-linked and proton leak OCR (with OLIGOmycin). Middle and right panels: OCR time course of immortalized WT and UCP1 KO browned adipocytes normalized to non-mitochondrial OCR (with ROTenone/Antimycin A). Port A: injection of compounds.

(L) Mean values of compound-induced OCR (isoproterenol [ISO-1 μM], oleoyl-L-leucine [18-1-Leu; 50 μM], or oleate [50 μM]).

(M–O) Proton leak OCR (M), coupling efficiency (N), and ATP synthesis-linked OCR (O) (n = 10–12 wells of two independent experiments).

All data represent means ± SEM. Statistical differences ($p < 0.05$) are indicated by different letters. See also Figures S2–S4.

(Figure 4M). Calculation of the coupling efficiency demonstrates that oleoyl-L-leucine dissipates 80% of oxidative energy as heat irrespective of UCP1 (Figure 4N), and this is further enhanced in combination with isoproterenol (Figure S4H). Isoproterenol on its own does not change coupling efficiency, suggesting virtually no increase in proton permeability. The induced OCR results from increased ATP-linked respiration (Figure 4O), which reports additional ATP consuming processes. Whether this enhanced ATP turnover, contributing to about 50% of cellular thermogenesis, is linked to futile lipid cycling or to creatine cycling, as suggested by others (Bertholet et al., 2017; Kazak et al., 2015), remains to be determined. However, additional ATP demand may simply derive from increased lipolysis where cAMP has to be synthesized or fatty acids have to be activated.

Summary and Conclusion

Previously, we and others have suggested a profound importance for FGF21 during cold-induced thermogenesis (Chartoumpekis et al., 2011; Fisher et al., 2012; Hanssen et al., 2015; Hondares et al., 2011; Keipert et al., 2015; Lee et al., 2013, 2014). However, to our best knowledge, this is the first report analyzing in detail the effect of genetic FGF21 loss during long-term cold adaptation. Unexpectedly, the lack of FGF21 does not lead to any difference in energy metabolism and adipose thermogenic gene regulation during cold acclimation, in contrast to earlier statements (Fisher et al., 2012). Exaggerated FGF21 release from ''non-thermogenic'' BAT of UCP1 KO mice below thermoneutrality (Keipert et al., 2015; Samms et al., 2015) suggests compensatory thermoregulatory mechanisms. However, the dKO mouse sustains normal body temperature throughout cold acclimation. Remarkably, the remodeling of inguinal WAT occurs in the absence of FGF21.

The data of our study demonstrate a negligible role of FGF21 for the maintenance of metabolic homeostasis in the cold, even in the absence of UCP1. UCP1- and FGF21-independent browning of iWAT appears to be associated with genes that have been implicated in futile cycling of lipids and endogenous uncoupling mechanisms (Long et al., 2016; Rohm et al., 2016). The significance of these alternative thermogenic mechanisms *in vivo*, except for muscle shivering, may require adequate mouse models with specific inactivation of alternative thermogenic pathways in adipose tissues. However, no quantitative differences in energy expenditure were observed in the absence of UCP1 and FGF21, suggesting alternative thermogenic pathways that are able to maintain body temperature with an efficiency equal to that of classical BAT thermogenesis. Further investigation may address whether these are beneficial for metabolic health, e.g., through specific lipid clearance by brown and beige adipose tissue (Bartelt et al., 2011). Thus, our study should be important to expand translational research on UCP1 and FGF21 biology to treat obesity and diabetes.

STAR★METHODS

Detailed methods are provided in the online version of this paper and include the following:

- KEY RESOURCES TABLE
- CONTACT FOR REAGENT AND RESOURCE SHARING
- EXPERIMENTAL MODEL AND SUBJECT DETAILS
  - Animals
- METHOD DETAILS
  - Indirect Calorimetry and Body Temperature Telemetry
  - Serum Analysis
  - Histology
  - DAPI and Nile Red Staining and Microscopy
  - Gene Expression Analysis
  - Transcriptomic Analysis
  - Western Blotting
  - N-Acyl Amino Acid Synthesis
  - Isolation and Immortalization of Murine Inguinal White Adipocytes
  - Seahorse Experiments
- QUANTIFICATION AND STATISTICAL ANALYSIS

SUPPLEMENTAL INFORMATION

Supplemental Information includes four figures and one table and can be found with this article online at http://dx.doi.org/10.1016/j.cmet.2017.07.016.

AUTHOR CONTRIBUTIONS

S.K. and M.K. performed animal experiments and collected and analyzed the data, except histology (by L.B. and F.N.), serum analysis (by S.H.), and RNA sequencing (by T.S. and E.G.). M.O. and E.M.v.S. performed bioinformatical analyses of RNA-seq data and interpreted the data with S.K. S.E.M. and D.L. performed part of the in vitro work on adipocytes. I.H. and O.P. synthesized N-acyl amino acids. M.H.T. and S.L. contributed reagents/materials/analytic tools and gave advice on experimental design. M.J. and S.K. conceptualized and designed the study and drafted, wrote, and edited the manuscript, which was substantially edited by all authors.

ACKNOWLEDGMENTS

We thank Sandy Lösecke for excellent technical assistance. This work was supported by a grant to S.K. and S.H. from the German Center for Diabetes Research (DZD) and supported in part by funding to M.H.T. from the Alexander von Humboldt Foundation, the Helmholtz Alliance ICEMED and the Helmholtz Initiative on Personalized Medicine iMed by Helmholtz Association, and the Helmholtz cross-program topic ''Metabolic Dysfunction.'' The Graphical Abstract was created using Servier Medical Art (http://www.servier.com).

Received: November 8, 2016
Revised: May 31, 2017
Accepted: July 18, 2017
Published: August 1, 2017

REFERENCES

Anders, S., Pyl, P.T., and Huber, W. (2015). HTSeq–a Python framework to work with high-throughput sequencing data. Bioinformatics *31*, 166–169.

Aydin, J., Shabalina, I.G., Place, N., Reiken, S., Zhang, S.J., Bellinger, A.M., Nedergaard, J., Cannon, B., Marks, A.R., Bruton, J.D., and Westerblad, H. (2008). Nonshivering thermogenesis protects against defective calcium handling in muscle. FASEB J. *22*, 3919–3924.

Badman, M.K., Koester, A., Flier, J.S., Kharitonenkov, A., and Maratos-Flier, E. (2009). Fibroblast growth factor 21-deficient mice demonstrate impaired adaptation to ketosis. Endocrinology *150*, 4931–4940.

Bartelt, A., Bruns, O.T., Reimer, R., Hohenberg, H., Ittrich, H., Peldschus, K., Kaul, M.G., Tromsdorf, U.I., Weller, H., Waurisch, C., et al. (2011). Brown adipose tissue activity controls triglyceride clearance. Nat. Med. *17*, 200–205.

Bertholet, A.M., Kazak, L., Chouchani, E.T., Bogaczyńska, M.G., Paranjpe, I., Wainwright, G.L., Bétourné, A., Kajimura, S., Spiegelman, B.M., and Kirichok, Y. (2017). Mitochondrial Patch Clamp of Beige Adipocytes Reveals

UCP1-Positive and UCP1-Negative Cells Both Exhibiting Futile Creatine Cycling. Cell Metab. *25*, 811–822.e4.

Cannon, B., and Nedergaard, J. (2004). Brown adipose tissue: function and physiological significance. Physiol. Rev. *84*, 277–359.

Chartoumpekis, D.V., Habeos, I.G., Ziros, P.G., Psyrogiannis, A.I., Kyriazopoulou, V.E., and Papavassiliou, A.G. (2011). Brown adipose tissue responds to cold and adrenergic stimulation by induction of FGF21. Mol. Med. *17*, 736–740.

Coskun, T., Bina, H.A., Schneider, M.A., Dunbar, J.D., Hu, C.C., Chen, Y., Moller, D.E., and Kharitonenkov, A. (2008). Fibroblast growth factor 21 corrects obesity in mice. Endocrinology *149*, 6018–6027.

Dobin, A., Davis, C.A., Schlesinger, F., Drenkow, J., Zaleski, C., Jha, S., Batut, P., Chaisson, M., and Gingeras, T.R. (2013). STAR: ultrafast universal RNA-seq aligner. Bioinformatics *29*, 15–21.

Fabbiano, S., Suárez-Zamorano, N., Rigo, D., Veyrat-Durebex, C., Stevanovic Dokic, A., Colin, D.J., and Trajkovski, M. (2016). Caloric Restriction Leads to Browning of White Adipose Tissue through Type 2 Immune Signaling. Cell Metab. *24*, 434–446.

Fisher, F.M., Kleiner, S., Douris, N., Fox, E.C., Mepani, R.J., Verdeguer, F., Wu, J., Kharitonenkov, A., Flier, J.S., Maratos-Flier, E., and Spiegelman, B.M. (2012). FGF21 regulates PGC-1α and browning of white adipose tissues in adaptive thermogenesis. Genes Dev. *26*, 271–281.

Golozoubova, V., Hohtola, E., Matthias, A., Jacobsson, A., Cannon, B., and Nedergaard, J. (2001). Only UCP1 can mediate adaptive nonshivering thermogenesis in the cold. FASEB J. *15*, 2048–2050.

Granneman, J.G., Burnazi, M., Zhu, Z., and Schwamb, L.A. (2003). White adipose tissue contributes to UCP1-independent thermogenesis. Am. J. Physiol. Endocrinol. Metab. *285*, E1230–E1236.

Guan, H.P., Li, Y., Jensen, M.V., Newgard, C.B., Steppan, C.M., and Lazar, M.A. (2002). A futile metabolic cycle activated in adipocytes by antidiabetic agents. Nat. Med. *8*, 1122–1128.

Haemmerle, G., Moustafa, T., Woelkart, G., Büttner, S., Schmidt, A., van de Weijer, T., Hesselink, M., Jaeger, D., Kienesberger, P.C., Zierler, K., et al. (2011). ATGL-mediated fat catabolism regulates cardiac mitochondrial function via PPAR-α and PGC-1. Nat. Med. *17*, 1076–1085.

Hanssen, M.J., Broeders, E., Samms, R.J., Vosselman, M.J., van der Lans, A.A., Cheng, C.C., Adams, A.C., van Marken Lichtenbelt, W.D., and Schrauwen, P. (2015). Serum FGF21 levels are associated with brown adipose tissue activity in humans. Sci. Rep. *5*, 10275.

Hondares, E., Iglesias, R., Giralt, A., Gonzalez, F.J., Giralt, M., Mampel, T., and Villarroya, F. (2011). Thermogenic activation induces FGF21 expression and release in brown adipose tissue. J. Biol. Chem. *286*, 12983–12990.

Hotta, Y., Nakamura, H., Konishi, M., Murata, Y., Takagi, H., Matsumura, S., Inoue, K., Fushiki, T., and Itoh, N. (2009). Fibroblast growth factor 21 regulates lipolysis in white adipose tissue but is not required for ketogenesis and triglyceride clearance in liver. Endocrinology *150*, 4625–4633.

Inagaki, T., Dutchak, P., Zhao, G., Ding, X., Gautron, L., Parameswara, V., Li, Y., Goetz, R., Mohammadi, M., Esser, V., et al. (2007). Endocrine regulation of the fasting response by PPARalpha-mediated induction of fibroblast growth factor 21. Cell Metab. *5*, 415–425.

Jastroch, M., Hirschberg, V., and Klingenspor, M. (2012). Functional characterization of UCP1 in mammalian HEK293 cells excludes mitochondrial uncoupling artefacts and reveals no contribution to basal proton leak. Biochim. Biophys. Acta *1817*, 1660–1670.

Kazak, L., Chouchani, E.T., Jedrychowski, M.P., Erickson, B.K., Shinoda, K., Cohen, P., Vetrivelan, R., Lu, G.Z., Laznik-Bogoslavski, D., Hasenfuss, S.C., et al. (2015). A creatine-driven substrate cycle enhances energy expenditure and thermogenesis in beige fat. Cell *163*, 643–655.

Kazak, L., Chouchani, E.T., Stavrovskaya, I.G., Lu, G.Z., Jedrychowski, M.P., Egan, D.F., Kumari, M., Kong, X., Erickson, B.K., Szpyt, J., et al. (2017). UCP1 deficiency causes brown fat respiratory chain depletion and sensitizes mitochondria to calcium overload-induced dysfunction. Proc. Natl. Acad. Sci. USA, 201705406.

Keipert, S., and Jastroch, M. (2014). Brite/beige fat and UCP1 - is it thermogenesis? Biochim. Biophys. Acta *1837*, 1075–1082.

Keipert, S., Kutschke, M., Lamp, D., Brachthäuser, L., Neff, F., Meyer, C.W., Oelkrug, R., Kharitonenkov, A., and Jastroch, M. (2015). Genetic disruption of uncoupling protein 1 in mice renders brown adipose tissue a significant source of FGF21 secretion. Mol. Metab. *4*, 537–542.

Kharitonenkov, A., Shiyanova, T.L., Koester, A., Ford, A.M., Micanovic, R., Galbreath, E.J., Sandusky, G.E., Hammond, L.J., Moyers, J.S., Owens, R.A., et al. (2005). FGF-21 as a novel metabolic regulator. J. Clin. Invest. *115*, 1627–1635.

Kharitonenkov, A., Wroblewski, V.J., Koester, A., Chen, Y.F., Clutinger, C.K., Tigno, X.T., Hansen, B.C., Shanafelt, A.B., and Etgen, G.J. (2007). The metabolic state of diabetic monkeys is regulated by fibroblast growth factor-21. Endocrinology *148*, 774–781.

Lee, P., Brychta, R.J., Linderman, J., Smith, S., Chen, K.Y., and Celi, F.S. (2013). Mild cold exposure modulates fibroblast growth factor 21 (FGF21) diurnal rhythm in humans: relationship between FGF21 levels, lipolysis, and cold-induced thermogenesis. J. Clin. Endocrinol. Metab. *98*, E98–E102.

Lee, P., Linderman, J.D., Smith, S., Brychta, R.J., Wang, J., Idelson, C., Perron, R.M., Werner, C.D., Phan, G.Q., Kammula, U.S., et al. (2014). Irisin and FGF21 are cold-induced endocrine activators of brown fat function in humans. Cell Metab. *19*, 302–309.

Long, J.Z., Svensson, K.J., Bateman, L.A., Lin, H., Kamenecka, T., Lokurkar, I.A., Lou, J., Rao, R.R., Chang, M.R., Jedrychowski, M.P., et al. (2016). The Secreted Enzyme PM20D1 Regulates Lipidated Amino Acid Uncouplers of Mitochondria. Cell *166*, 424–435.

Love, M.I., Huber, W., and Anders, S. (2014). Moderated estimation of fold change and dispersion for RNA-seq data with DESeq2. Genome Biol. *15*, 550.

Matsushita, M., Yoneshiro, T., Aita, S., Kameya, T., Sugie, H., and Saito, M. (2014). Impact of brown adipose tissue on body fatness and glucose metabolism in healthy humans. Int. J. Obes. *38*, 812–817.

Meyer, C.W., Willershäuser, M., Jastroch, M., Rourke, B.C., Fromme, T., Oelkrug, R., Heldmaier, G., and Klingenspor, M. (2010). Adaptive thermogenesis and thermal conductance in wild-type and UCP1-KO mice. Am. J. Physiol. Regul. Integr. Comp. Physiol. *299*, R1396–R1406.

Mottillo, E.P., Balasubramanian, P., Lee, Y.H., Weng, C., Kershaw, E.E., and Granneman, J.G. (2014). Coupling of lipolysis and de novo lipogenesis in brown, beige, and white adipose tissues during chronic β3-adrenergic receptor activation. J. Lipid Res. *55*, 2276–2286.

Nedergaard, J., Bengtsson, T., and Cannon, B. (2007). Unexpected evidence for active brown adipose tissue in adult humans. Am. J. Physiol. Endocrinol. Metab. *293*, E444–E452.

Oelkrug, R., Kutschke, M., Meyer, C.W., Heldmaier, G., and Jastroch, M. (2010). Uncoupling protein 1 decreases superoxide production in brown adipose tissue mitochondria. J. Biol. Chem. *285*, 21961–21968.

Ost, M., Coleman, V., Voigt, A., van Schothorst, E.M., Keipert, S., van der Stelt, I., Ringel, S., Graja, A., Ambrosi, T., Kipp, A.P., et al. (2015). Muscle mitochondrial stress adaptation operates independently of endogenous FGF21 action. Mol. Metab. *5*, 79–90.

Rohm, M., Schäfer, M., Laurent, V., Üstünel, B.E., Niopek, K., Algire, C., Hautzinger, O., Sijmonsma, T.P., Zota, A., Medrikova, D., et al. (2016). An AMP-activated protein kinase-stabilizing peptide ameliorates adipose tissue wasting in cancer cachexia in mice. Nat. Med. *22*, 1120–1130.

Samms, R.J., Smith, D.P., Cheng, C.C., Antonellis, P.P., Perfield, J.W., 2nd, Kharitonenkov, A., Gimeno, R.E., and Adams, A.C. (2015). Discrete Aspects of FGF21 In Vivo Pharmacology Do Not Require UCP1. Cell Rep. *11*, 991–999.

Schulz, T.J., Huang, P., Huang, T.L., Xue, R., McDougall, L.E., Townsend, K.L., Cypess, A.M., Mishina, Y., Gussoni, E., and Tseng, Y.H. (2013). Brown-fat paucity due to impaired BMP signalling induces compensatory browning of white fat. Nature *495*, 379–383.

Shabalina, I.G., Hoeks, J., Kramarova, T.V., Schrauwen, P., Cannon, B., and Nedergaard, J. (2010). Cold tolerance of UCP1-ablated mice: a skeletal muscle mitochondria switch toward lipid oxidation with marked UCP3 up-regulation not associated with increased basal, fatty acid- or ROS-induced

uncoupling or enhanced GDP effects. Biochim. Biophys. Acta *1797*, 968–980.

Shabalina, I.G., Petrovic, N., de Jong, J.M., Kalinovich, A.V., Cannon, B., and Nedergaard, J. (2013). UCP1 in brite/beige adipose tissue mitochondria is functionally thermogenic. Cell Rep. *5*, 1196–1203.

Stier, A., Bize, P., Habold, C., Bouillaud, F., Massemin, S., and Criscuolo, F. (2014). Mitochondrial uncoupling prevents cold-induced oxidative stress: a case study using UCP1 knockout mice. J. Exp. Biol. *217*, 624–630.

Ukropec, J., Anunciado, R.P., Ravussin, Y., Hulver, M.W., and Kozak, L.P. (2006). UCP1-independent thermogenesis in white adipose tissue of cold-acclimated Ucp1-/- mice. J. Biol. Chem. *281*, 31894–31908.

Vitali, A., Murano, I., Zingaretti, M.C., Frontini, A., Ricquier, D., and Cinti, S. (2012). The adipose organ of obesity-prone C57BL/6J mice is composed of mixed white and brown adipocytes. J. Lipid Res. *53*, 619–629.

Wickham, H. (2009). ggplot2: Elegant Graphics for Data Analysis (Springer-Verlag New York).

STAR★METHODS

KEY RESOURCES TABLE

REAGENT or RESOURCE	SOURCE	IDENTIFIER
Antibodies		
total oxphos antibody	Thermo Fisher	Cat. No. 458099; RRID: AB_2533835
alpha tubulin	Santa Cruz Biotechnology	SC-23948; RRID: AB_628410
UCP1	Customized rabbit antibody raised against hamster (*Phodopus sungorus*) UCP1	Jastroch et al., 2012
Chemicals, Peptides, and Recombinant Proteins		
Insulin	Sigma	Cat. No. I9278
Rosiglitazone	VWR	Cat. No. CAYM71740-10
Isoproterenol	Sigma	Cat. No. I6504
IBMX	Sigma	Cat. No. 15879
Dexamethasone	Sigma	Cat. No. D1756
Oligomycin	Sigma	Cat. No. O4876
DNP	Sigma	Cat. No. 34334
Rotenone	Sigma	Cat. No. R8875
Antimycin A (AA)	Sigma	Cat. No. A8674
Oleate	Sigma	Cat. No. O7501
N-acyl amino acids	This paper	N/A
Critical Commercial Assays		
Intact FGF-21 ELISA Kit	Eagle Biosciences	Cat. No. F2131-K01
TG Colorimetric Assay Kit	Cayman	Cat. No. 10010303
Glycerol Colorimetric Assay Kit	Biomol	Cat. No. Cay10010755-96
NEFA-HR2	Wako Chemicals	Cat. No. 435-91795/436-91995
Cholesterol Fluometric Assay Kit	VWR International	Cat. No. CAYM10007640-1
Bio-Plex Pro Mouse Diabetes Adiponectin Assay	Bio-Rad	Cat. No. 171-F7002M
Bio-Plex Pro Mouse Cytokine 23-plex Assay	Bio-Rad	Cat. No. M60-009RDPD
MILLIPLEX MAP Mouse Myokine Magnetic Bead Panel	Millipore	Cat. No. MMYOMAG-74K-12
RNA 6000 Nano Kit	Agilent	Cat. No. 5067-1511
Quant-iT PicoGreen dsDNA Assay Kit	Life Technologies	Cat. No. P11496
Experimental Models: Cell Lines		
Immortalized white adipose tissue cell line	This paper, SV40 Virus	
Experimental Models: Organisms/Strains		
UCP1 KO mice (B6.129-UCP1$^{tmkz/j}$)	The Jackson Laboratory	Stock No. 003124
FGF21 KO mice	Lab of Nobuyuki Itoh	Hotta et al., 2009
Oligonucleotides		
Primers for RT-PCR, see Table S1	This paper	N/A
Software and Algorithms		
GraphPad prism 6.0b	GraphPad	N/A
HTseq-count	Anders et al., 2015	https://pypi.python.org/pypi/HTSeq
R Bioconductor package DESeq2	Love et al., 2014	https://bioconductor.org/packages/release/bioc/html/DESeq2.html
R package ggplot2 and the stat_ellipse method	Wickham, 2009	http://ggplot2.org/

(*Continued on next page*)

Continued		
REAGENT or RESOURCE	SOURCE	IDENTIFIER
Venny 2.1	Oliveros, J.C.	http://bioinfogp.cnb.csic.es/tools/venny/index.html
MetaCore	Thomson Reuters	version 6.30.68780
Others		
Indirect calorimetry system - TSE PhenoMaster	TSE Systems Germany	N/A
VitalView Data Acquisition System	Mini Mitter Co.	N/A
RNA sequencing data of Keipert et al., 2017 (this study)	GEO	GSE99412

CONTACT FOR REAGENT AND RESOURCE SHARING

As Lead Contact, Martin Jastroch is responsible for all reagent and resource requests. Please contact Martin Jastroch at martin.jastroch@helmholtz-muenchen.de with requests and inquiries.

EXPERIMENTAL MODEL AND SUBJECT DETAILS

Animals

The experiments were performed in homozygous, male wild-type (WT), FGF21 KO, UCP1 KO and UCP1-FGF12 double KO (dKO) mice (genetic background C57BL/6J). We reduced confounding developmental adaptation to thermal stress by breeding, raising and maintaining all mice at thermoneutrality before experimental procedures. The breeding strategy was performed as following: In the first breeding round, homozygous UCP1 KO mice were bred with homozygous FGF21 KO mice to generate heterozygous UCP1/FGF21 KO mice. The resulting heterozygous mice were mated to generate homozygous mice of all genoytpes, which were again mated and used for the experiment. Mice were housed in groups with ad libitum access to food and water in a 12:12-hr dark-light cycle (lights on:7:00 CET). All animal experiments were conducted under the guidelines of the Institutional Animal Care and Committee of the Helmholtz Center Munich approved animal maintenance and experimental procedures.

METHOD DETAILS

Indirect Calorimetry and Body Temperature Telemetry

At the age of 9-10 weeks, each mouse was anesthetized, and a temperature-sensitive transmitter (G2 E-Mitter) was implanted intra-abdominally. Mice were allowed to recover for a minimum of seven days after implantation. At the age of 10 to 12 weeks, mice were transferred to a temperature-controlled (±0.5°C) climate chamber and placed on telemetry receivers (TR 3000, Mini Mitter) for the time period of 6 weeks. Core body temperature was continuously monitored with a VitalView Data Acquisition System (Mini Mitter Co., Sunriver, USA). The signal emitted by the transmitter was received and converted into temperature by VitalView software. Energy expenditure, food intake, activity and respiratory quotient (RQ = CO_2 produced/O_2 consumed) were measured by indirect calorimetry using an open respirometry system with the simultaneous measurement of activity, food and water intake (TSE PhenoMaster, TSE Systems, Germany). Measurements were performed in 10 min intervals over a period of 6 weeks. Afterward, mice were euthanized after 2-3 hr food withdrawal, and serum and tissue samples were collected. The last two days of each temperature step were analyzed to assess genotypic differences of metabolic cold adaptation, avoiding acute cold stress effects.

Serum Analysis

For all serum analyses, commercially available assay kits were used according to the manufacturer's recommendations. FGF21 serum analyses (intact FGF21 Elisa Kit, Eagle Biosciences), serum triglycerides (TG Calorimetric Assay Kit, Cayman), and glycerol (Glycerol Colorimetric Assay Kit, Biomol) were measured undiluted. For NEFA (NEFA-HR2 Wako Chemicals) detection, serum was diluted 1:2, for Cholesterol 1:300 (Fluometric Assay Kit, Cayman) and for Adiponectin 1:1600 (Bio-Plex Pro Mouse Diabetes Adiponectin Assay, Bio-Rad). For cytokine detection, the Bio-Plex Pro Mouse Cytokine 23-plex Assay (Bio-Rad) and the MILLIPLEX MAP Mouse Myokine Magnetic Bead Panel (Millipore) were used. Serum samples were stored at −80°C until use.

Histology

BAT and WAT pieces were fixed in 4% paraformaldehyde (Roth Chemicals) for 24 hr and embedded in low melting paraffin (Paraplast Plus, Sigma Aldrich). Four-μm-thick sections were cut (rotary microtome HSM55, Microm) and sections were mounted, dehydrated in increasing ethanol series and stained with hematoxylin and eosin (H&E) (Merck). Bright field images were taken with the Keyence Microscope BZ-9000.

DAPI and Nile Red Staining and Microscopy

Adipocytes were fixed with 4% PFA at differentiation day 6, then stained with Dapi (nuclei; blue, 1:5000 dilution of 5 mg/mL stock) and Nile red (Lipid droplets; green, 1:250 dilution of 1 mg/mL stock) for 2 hr at 37°C before washing twice with PBS. Bright-field and fluorescence microscopy was performed with a Keyence BZ-9000 microscope.

Gene Expression Analysis

RNA isolation and quantitative real-time PCR were performed as described previously (Keipert et al., 2015). Gene expression of different tissues in Figures 1A and 1B was calculated to respective Ct-values without normalization to WT or tissue-specific housekeeping genes, thus allowing for multi-tissue comparisons. Gene expression in all other figures was calculated as ddCT, using *Hprt* or B2 microglobulin (*B2m*) for normalization and relative to the WT control group, which was normalized to a value of 1. The oligonucleotide primer sequences are shown in Table S1.

Transcriptomic Analysis

Total RNA was extracted from inguinal WAT, BAT, muscle and hypothalamus of WT, FGF21 KO, UCP1 KO and dKO mice (n = 5-6) using Qiazol according to the manufacturer's instructions (Qiazol Lysis Reagent, QIAGEN). The quality of the RNA was determined with the Agilent 2100 BioAnalyzer (RNA 6000 Nano Kit, Agilent). All samples had a RNA integrity number (RIN) value greater than 8. For library preparation, 1 μg of total RNA per sample was used. RNA molecules were poly(A) selected, fragmented, and reverse transcribed with the Elute, Prime, Fragment Mix (EPF, Illumina). End repair, A-tailing, adaptor ligation, and library enrichment were performed as described in the TruSeq Stranded mRNA Sample Preparation Guide (Illumina). RNA libraries were assessed for quality and quantity with the Agilent 2100 BioAnalyzer and the Quant-iT PicoGreen dsDNA Assay Kit (Life Technologies). Strand-specific RNA libraries were sequenced as 100 bp paired-end runs on an Illumina HiSeq4000 platform. On average we produced about 8.5 Gb of sequence per sample. The STAR aligner (Dobin et al., 2013) with modified parameter settings (–two pass Mode = Basic) was used for split-read alignment against the mouse genome assembly mm10 (GRCm38) and UCSC known Gene annotation. To quantify the number of reads mapping to annotated genes we used HTseq-count (Anders et al., 2015). The Relative Log Expression (RLE) normalization implemented in the R Bioconductor package DESeq2 (Love et al., 2014) was used to normalize gene counts. PCA plots were created with the R package ggplot2 and the stat_ellipse method (Wickham, 2009) and Venn diagrams were created using the significant regulated transcripts between WT and FGF21KO/UCP1KO/dKO (for BAT, iWAT, Muscle FDR-adjusted $p < 0.05$, FC ≥ 1.2; for Hypothalamus FDR-adjusted $p < 0.05$, FC ≥ 1.1) using Venny 2.1 (Oliveros, J.C.; Venny. An interactive tool for comparing lists with Venn's diagrams: http://bioinfogp.cnb.csic.es/tools/venny/index.html).

Enrichment analysis of metabolic and process networks as well as pathways, using transcripts with a FDR-adjusted $p < 0.05$, was performed using MetaCore (version 6.30.68780, Thomson Reuters, New York, NY, USA). Top 30 upregulated and downregulated unique and known protein-encoded transcripts between UCP1 KO and WT were identified and compared for expression levels with the FGF21 KO and dKO mice. Heatmaps were constructed within GeneMaths XT 2.12 (Applied Maths, Sint-Martens-Latem, Belgium) using hierarchical clustering based on linear scaled Euclidean distance analysis using Unweighted Pair Group Method with Arithmetic Mean (UPGMA) for both samples and transcripts. The accession number for the sequencing data reported in this paper is GEO: GSE79423.

Western Blotting

For protein extraction tissue was homogenized in RIPA buffer (150 mM NaCl, 50 mM TRIS, 0.1% SDS, 1% IGEPAL CA-630, 0.5% Sodium deoxycholate; pH 7.4-7.6) containing protease inhibitor cocktail (Halt TM Protease & Phosphatase Inhibitor Cocktail, Thermo Scientific) and protein concentration was measured using Bradford reagent (Sigma). The following primary antibodies were used: UCP1 (rabbit anti-hamster UCP1), alpha tubulin (Santa Cruz Biotechnology) and total oxphos antibody (Thermo Fisher). Horseradish-peroxidase-conjugated secondary antibodies were used: anti-rabbit IgG (Santa Cruz Biotechnology) or anti-mouse IgG (Santa Cruz Biotechnology).

N-Acyl Amino Acid Synthesis

^{1}H and ^{13}C NMR spectra were obtained on Bruker spectrometers (Ascend and Ultrashield) in the indicated solvent. Column chromatography was carried out on a Büchi Reveleris PREP. HR-MS were measured on a Q-Tof Premier (Waters) with lockspray ion source (ESI, positive ions) coupled to an Acquity UPLC system (Waters). Commercially available chemicals and solvents were used as received.

Amide Coupling: Oleic acid (1.1 eq.) was dissolved in 5 mL DMF/CH_2Cl_2 (1:2) and Oxyma (1.2 eq.), 1-Ethyl-3-(3-dimethylaminopropyl)carbodiimide hydrochloride (1.1 eq.) and sodium bicarbonate (5 eq.) were added. After 5 min of stirring at room temperature amino acid as methyl ester (1 eq., 300 mg) was added and the reaction mixture was stirred at room temperature until the reaction was complete. The organic phase was extracted with 1 M hydrochloric acid, saturated sodium bicarbonate and brine and dried over sodium sulfate. The solvent was removed under reduced pressure to obtain the crude product. The crude was purified via reversed phase flash chromatography (H_2O/MeCN + 0.05% TFA; 5 → 95% MeCN) to obtain the pure product. Saponification: Oleoyl amino acid was dissolved in tetrahydrofuran (0.1 M) and 1 M lithium hydroxide (1.1 eq.) was added. After completion of the ester cleavage,

the pH was adjusted to pH 2–3 by addition of 1 M potassium hydrogen sulfate and the mixture was extracted with ethyl acetate. The combined organic layers were dried over sodium sulfate, the solvent was removed under reduced pressure and the crude product was lyophilized. No purification was required.

Methyl Oleoyl-L-leucinate

Starting from methyl L-leucinate hydrochloride, methyl oleoyl-L-leucinate was synthesized via the general procedure for amide coupling. ^{1}H NMR (400 MHz, $CDCl_3$) δ (ppm): 0.88 (t, 3 H, J = 6.9 Hz), 0.91 – 0.96 (m, 6 H), 1.20 – 1.38 (m, 20 H), 1.47 – 1.57 (m, 1 H), 1.58 – 1.69 (m, 4 H), 1.95 – 2.05 (m, 2 H), 2.22 (t, 2 H, J = 7.7 Hz), 3.73 (s, 3 H), 4.66 (dt, 1 H, J = 4.9, 8.7 Hz), 5.29 – 5.40 (m, 2 H), 5.80 (d, 1 H, J = 8.2 Hz); ^{13}C NMR (400 MHz, $CDCl_3$) δ (ppm): 14.3, 22.1, 22.8, 22.9, 25.0, 25.7, 27.3, 27.4, 29.3, 29.3, 29.4, 29.5, 29.5, 29.7, 29.8, 29.9, 32.1, 36.7, 42.0, 50.7, 52.4, 129.9, 130.1, 173.2, 173.9; HR-MS (ESI-TOF): m/z: $[M+Na]^+$: Calcd. for $C_{25}H_{47}NO_3Na$: 432.3454; found: 432.3451.

Oleoyl-L-leucine

Starting from methyl oleoyl-L-leucinate (47 mg, 0.115 mmol), Oleoyl-L-leucine was synthesized via the general procedure for saponification. ^{1}H NMR (400 MHz, $CDCl_3$) δ (ppm): 0.88 (t, 3 H, J = 6.8 Hz), 0.94 – 0.98 (m, 6 H), 1.18 – 1.39 (m, 20 H), 1.53 – 1.79 (m, 5 H), 1.92 – 2.07 (m, 4 H), 2.24 (dd, 2 H, J = 7.7 Hz), 4.56 – 4.64 (m, 1 H), 5.29 – 5.40 (m, 2 H), 5.81 (d, 1 H, J = 7.8 Hz); ^{13}C NMR (400 MHz, $CDCl_3$) δ (ppm): 14.3, 22.0, 22.8, 23.0, 25.0, 25.7, 27.3, 27.4, 29.3, 29.3, 29.4, 29.5, 29.5, 29.7, 29.8, 29.9, 32.1, 36.6, 41.1, 51.0, 129.9, 130.2, 174.2, 175.9; HR-MS (ESI-TOF): m/z: $[M+Na]^+$: Calcd. for $C_{24}H_{45}NO_3Na$: 418.3297; found: 418.3293.

Methyl Oleoyl-L-phenylalaninate

Starting from methyl L-phenylalaninate hydrochloride, methyl oleoyl-L-phenylalaninate was synthesized via the general procedure for amide coupling. ^{1}H NMR (400 MHz, $CDCl_3$) δ (ppm): 0.88 (t, 3 H, J = 6.8 Hz), 1.20 – 1.39 (m, 20 H), 1.53 – 1.63 (m, 2 H), 1.93 – 2.05 (m, 4 H), 2.13 – 2.20 (m, 2 H), 3.09 (dd, 1 H, J = 5.9, 13.9 Hz), 3.16 (dd, 1 H, J = 5.9, 13.9 Hz), 3.73 (s, 3 H), 4.91 (dt, 1 H, J = 5.8, 7.9 Hz), 5.29 – 5.40 (m, 2 H), 5.84 (d, 1 H, J = 7.6 Hz), 7.06 – 7.11 (m, 2 H), 7.21 – 7.31 (m, 3 H); ^{13}C NMR (400 MHz, $CDCl_3$) δ (ppm): 14.3, 22.8, 25.7, 27.3, 27.4, 29.3, 29.3, 29.4, 29.5, 29.5, 29.7, 29.9, 29.9, 32.1, 36.7, 38.1, 52.5, 53.0, 127.3, 128.7, 129.4, 129.9, 130.2, 136.0, 172.3, 172.8; HR-MS (ESI-TOF): m/z: $[M+Na]^+$: Calcd. for $C_{28}H_{45}NO_3Na$: 466.3297; found: 466.3294.

Oleoyl-L-phenylalanine

Starting from methyl oleoyl-L-phenylalaninate (40 mg, 0.09 mmol), oleoyl-L-phenylalanine was synthesized via the general procedure for saponification. ^{1}H NMR (400 MHz, $CDCl_3$) δ (ppm): 0.88 (t, 3 H, J = 6.9 Hz), 1.19 – 1.38 (m, 20 H), 1.50 – 1.62 (m, 2 H), 1.93 – 2.05 (m, 4 H), 2.14 – 2.21 (m, 2 H), 3.13 (dd, 1 H, J = 6.5, 14.1 Hz), 3.25 (dd, 1 H, J = 5.6, 14.2 Hz), 4.83 – 4.90 (m, 1 H), 5.29 – 5.41 (m, 2 H), 5.86 (d, 1 H, J = 7.4 Hz), 7.14 – 7.19 (m, 2 H), 7.23 – 7.34 (m, 3H); ^{13}C NMR (400 MHz, $CDCl_3$) δ (ppm): 14.3, 22.8, 25.6, 27.3, 27.4, 29.2, 29.3, 29.5, 29.5, 29.7, 29.9, 29.9, 32.1, 36.6, 37.3, 53.3, 53.4, 127.4, 128.9, 129.4, 129.9, 130.2, 135.7, 174.1, 174.3; HR-MS (ESI-TOF): m/z: $[M+Na]^+$: Calcd. for $C_{27}H_{43}NO_3Na$: 452.3141; found: 452.3139.

Isolation and Immortalization of Murine Inguinal White Adipocytes

The isolation of the stromal vascular (SV) fraction from the interscapular white adipose tissue (iWAT) pad of WT and UCP1 KO mice (6-8 weeks old) was performed as following: iWAT fat pads were minced and then digested for 30 min at 37°C (DMEM/F12 plus glutamax, 0.15% (w/v) collagenase Type IV, 2% BSA). The digested tissue was filtered through a 100 μm filter, and rinsed with DMEM/F12; thereafter cells were centrifuged at 400 g for 10 min. The pellet was washed once in 4 mL of Erythrocyte-Lysis buffer (154 mM NH_4Cl, 10 mM $KHCO_3$, 0.1 mM EDTA), incubated for 20 min and centrifuged again at 400 g for 10 min. Cells were re-suspended in growth media (DMEM/F12 plus glutamax, 10% FCS, 1% penicillin/streptomycin) plated and cultured. After 24 hr pre-adipocytes were immortalized by SV40 large T-antigen (a gift from Dr. Ussar). After another 48 hr cells were split into new flasks. Cells were allowed to grow to 60%–70% confluence and again split, or later frozen into aliquots using freezing media (Growth media, 10% DMSO).

Seahorse Experiments

Immortalized preadipocyte were plated onto XF96 V3 PET cell culture micro plates (Seahorse; 10K per well) and allowed to grow to 90%–100% confluence. At confluency, differentiation was started using a white fat differentiation cocktail (Growth media, 1 μM Dexamethasone, 0.5 mM IBMX, 1 μM Rosiglitazone, 5 μg/ml Insulin). At day 2 of differentiation, cells were exposed to growth medium (Growth media, 5 μg/ml Insulin) without (“white”) or with 1 μM rosiglitazone (“browned”) for another 4 days. On day six of differentiation cells were used for cell respiration assays. Before the measurements of cellular respiration, the cells were washed twice with assay medium (XF DMEM + 25 mM glucose) and then incubated in 180 μL of assay medium for 10 min in an air incubator without CO2 at 37°C. Oleate and Oleoyl-L-leucine were overnight equilibrated with 0.4% BSA and titrated. The XF96 plate was then transferred to the XF96 Extracellular Flux analyzer (Seahorse Bioscience). Four to five assay cycles (2 min mix, 2 min measuring period) were used to determine basal respiration. For the measurement of different mitochondrial respiration states, oligomycin (5 μg/ml) and dinitrophenol (DNP; 100μM) were used, and a cocktail containing rotenone (5 μM) and antimycin A (2 μM) served to correct for non-mitochondrial OCR. The N-Acyl amino acids as well as the oleate were diluted and equilibrated in XF DMEM + 0.5% BSA and incubated overnight on a shaker. The “ATP-linked respiration” represents the respiration rates prior to injection of oligomycin minus oligomycin-insensitive rates. Oligomycin- insensitive rates are labeled as “leak respiration.” The coupling efficiency represents the fraction of respiration used to drive ATP synthesis for each run, calculated as CE = ATP-linked/respiration prior to oligomycin-injection).

QUANTIFICATION AND STATISTICAL ANALYSIS

Statistical analyses were performed by Stat Graph Prism 6 (GraphPad Software, San Diego, CA USA). All data are reported as mean + SEM. After testing for equal distribution of the data and equal variances within the datasets, Student's t test (unpaired, 2-tailed), one-way or 2-way ANOVA and Bonferroni's multiple comparisons test was used to determine differences between the different genotypes/treatment groups and ambient temperatures. Statistical significance was assumed at $p < 0.05$. Statistical differences between different genotypes/treatment groups are indicated by letters, with means being significantly different indicated by different letters. Statistical significance of WT to UCP1 KO and dKO is denoted by WT *$p < 0.05$, WT **$p < 0.01$, WT ***$p < 0.001$ (gray dashed line indicates WT mean value).